AIAA Journal
Vol. 50, No. 8, August 2012

Physical Insight into Scramjet Inlet Behavior via Multi-Objective Design Optimization

Hideaki Ogawa* and Russell R. Boyce†
University of Queensland, Brisbane, Queensland 4072, Australia

DOI: 10.2514/1.J051644

Scramjet propulsion is a promising technology for reliable and economical access to space and high-speed atmospheric transport. The inlet plays a key role in determining the performance of scramjets, in particular for the axisymmetric class of scramjet engines that are currently explored due to their advantages in numerous aspects. In the present study, a multi-objective design optimization based on evolutionary algorithms has been conducted with respect to four major inlet design criteria, that is, compression efficiency, drag, adverse pressure gradient, and exit temperature, where the former three criteria are used as the objective functions and the last one is the constraint function. The flowfields have been examined for representative geometries, and sensitivity analysis has been performed with the aid of surrogate modeling, revealing the major impact of the inlet exit radius, advantages of Busemann-type geometries in various aspects, and direct correlation of the inlet drag, exit temperature, and surface-heat transfer. The insight gained here can be usefully applied to the design of high-performance scramjet inlets.

Nomenclature

A = cross-sectional area, m^2
$\mathrm{d}p/\mathrm{d}s$ = surface pressure gradient, Pa/m
F = point among feasible individuals
h = static enthalpy, J/kg
h_t = stagnation enthalpy, J/kg
l_i = length of ith ramp, m
$\dot{m}$ = mass flow, kg/s
O = point on Pareto optimal front
p = static pressure, Pa
R = specific gas constant, J/kg · K
r = radial coordinate or radius, m
S = first-order sensitivity index
S_T = total sensitivity index
s = coordinate along inlet surface, m
T = static temperature, K
x = streamwise coordinate, m
γ = specific heat ratio
ΔQ = heat transfer across inlet surface, J/s
$\Delta\theta_i$ = angle increment of ith ramp, deg
η_B = compression efficiency
θ = wall inclination, deg
θ_0 = first Mach wave angle of full Busemann inlet, deg
θ_i = angle of ith ramp, deg
τ = wall shear stress, N/m^2
$\bar{\chi}$ = stream-thrust-average value of parameter χ

Subscripts

c = property of combustor
isen = isentropic value
max = maximum value
pres = pressure component
rel. = relative value
t = property of leading-edge tip
visc = viscous component
1 = value at inlet entrance
2 = value at inlet exit
∞ = freestream value

I. Introduction

HYPERSONIC airbreathing propulsion offers the potential for reliable and economical transport for access to space and high-speed atmospheric cruise. In particular, scramjets (supersonic combustion ramjets) are a promising technology that can enable efficient and flexible transport systems, having marked significant milestones in the last decade: the world's first supersonic combustion in HyShot II Pprogram in July 2002 [1,2], the fastest atmospheric flights recorded by NASA's X-43A scramjet-powered vehicles in the Hyper-X program at Mach 6.8 (March 2004) and 9.6 (November 2004) [3], and the recent flight by the Boeing X-51A WaveRider, which recorded the longest scramjet burn duration of 140 s in May 2010 [4].

An axisymmetric scramjet configuration (Fig. 1) is currently being explored in ground and flight tests in Australia, following excellent performance demonstrated in shock tunnel testing [5,6]. Scramjet engines typically operate in a sequential process (Fig. 2): hypersonic inflow is captured and compressed through the inlet to the desired high pressure and temperature. Fuel is injected and mixed with air, and combustion takes place in the downstream chamber. The reacted gas is expanded by the nozzle to produce thrust. Combined with innovative concepts, including inlet fuel injection and radical-farming shock-induced combustion, the simple axisymmetric configuration can bring about numerous advantages over complex three-dimensional geometries in aerodynamic and combustion efficiency, aerothermal and structural management as well as manufacture [7,8].

Axisymmetric scramjet inlets with high internal compression, however, are inherently difficult to start spontaneously during flight and are highly susceptible to unstart. Numerical investigations have recently been conducted by the authors to address this issue and probe the underlying physics. Time-accurate computations have revealed a substantial influence of shock wave/boundary layer interactions on the inlet starting mechanism, with formation of separation at compression corners playing an essential role in the unstarting process [9]. Various techniques have been examined numerically to overcome the problem, where instantaneous diaphragm rupture (with bleed addition) and sliding doors (or

---

Received 29 September 2011; revision received 15 February 2012; accepted for publication 17 February 2012.

*Research Fellow, School of Mechanical and Mining Engineering, Centre for Hypersonics. Member AIAA.

†Professor, Defence Science and Technology Organization. Chair for Hypersonics, School of Mechanical and Mining Engineering, Centre for Hypersonics. Senior Member AIAA.

Fig. 1 Axisymmetric scramjet (upstream view) [6].

diaphragm erosion) have been found to be particularly effective in starting the inlets [10]. Despite the effectiveness of these methods, it is of crucial importance to design inlets that are naturally less susceptible to undesirable unstarting events for reliable and stable inflight operation of axisymmetric scramjets.

Design criteria for high-performance scramjet inlets typically include efficient compression with minimum viscous/shock losses, minimum contribution to the vehicle drag, and minimum adverse pressure gradient to prevent flow separation, while achieving adequate compression to induce ignition [11,12]. Such a design problem with multiple objectives would represent a formidable challenge for conventional gradient-based optimization approaches due to substantial complexity and nonlinearity introduced by highly coupled aerodynamic phenomena, including shock-shock interactions and shock wave/boundary layer interactions. Global search based on evolutionary algorithms is particularly suitable for the design of such complex systems that are characterized by nonlinear and nonsmooth design space being robust against the presence of local optimums [13]. The use of population-based search in aerospace design, however, would commonly entail prohibitive computational cost due to a large number of function evaluations [e.g., computational fluid dynamics (CFD), finite-element analysis] required in the course of heuristic search.

Surrogate modeling can efficiently mitigate the computational load by replacing expensive function evaluations with approximation from meta-analysis models [14,15]. The capability and robustness of surrogate-assisted evolutionary algorithms (SAEAs) in multi-objective optimization have been demonstrated for various test problems featuring multiple objectives and constraints and numerous decision variables, accurately capturing complex nondominated optimal fronts with minimum function evaluations [16,17]. SAEAs have been applied to design optimization problems for various aerospace applications, including turbomachinery, transonic aircraft, rocket engine components, and hypersonic nose cones [15,18–21]. More recently, an advanced SAEA-based multi-objective optimization capability coupled with state-of-the-art CFD codes has been applied to design problems of various components and full flow path of axisymmetric scramjet engines [22–25].

In the present research, a multi-objective design optimization with three objective functions and one constraint function has been performed for axisymmetric scramjet inlets to gain physical insight into the inlet flowfields. The optimization results and representative flowfields have been examined to investigate the key factors and underlying flow physics that can exert decisive influence on the inlet performance. The insight gained is described in a summary section intended to directly benefit the scramjet designer.

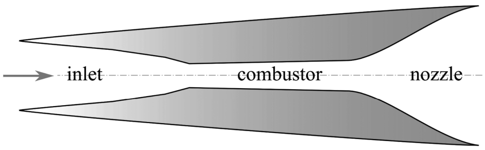

Fig. 2 Schematic of an axisymmetric scramjet.

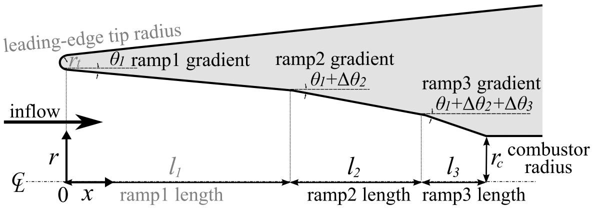

Fig. 3 Inlet design parameters.

II. Approaches

A. Configurations

1. Inlet Geometry

The inlet to be optimized in this paper comprises three ramps, as schematically shown in Fig. 3. The internal geometry is represented by eight parameters: the leading-edge nose-tip radius r_t, ramp lengths $l_{1,2,3}$, first ramp angle θ_1, ramp angle increments $\Delta\theta_{2,3}$, and exit radius r_c (or combustor radius). The baseline geometry is defined by the following values: $\theta_1 = 5.0$ deg, $\Delta\theta_2 = 5.3$ deg, $\Delta\theta_3 = 3.3$ deg, $l_1 = 0.204$ m, $l_2 = 0.069$ m, $l_3 = 0.039$ m, and $r_c = 0.035$ m. The inlet radius, which is measured from the axis of symmetry to the junction of the circular cross-sectional leading edge and the first inlet ramp, is fixed at 0.075 m to ensure constant mass flow entry, which effectively makes one of the ramp parameters dependent on the others for a given value of the combustor radius r_c (l_1 is rendered to be such a dependent variable in this study). Also fixed is the leading-edge nose-tip radius $r_t = 0.5$ mm to focus on the influence of ramp geometries by freezing the entropy-layer effect originating from the leading edge. These assumptions, in effect, leave six parameters (l_2, l_3, θ_1, $\Delta\theta_2$, $\Delta\theta_3$, and r_c) as design variables, or decision variables for optimization.

2. Flow Conditions

The freestream conditions are $M_\infty = 8.0$, $p_\infty = 1197$ Pa, and $T_\infty = 226.5$ K, assuming scramjet operation on a constant dynamic pressure trajectory of 53.6 kPa, at an altitude of 30 km. The rate of the mass flow captured by the constant inlet area is 0.78 kg/s. The Reynolds number based on the inlet radius (0.075 m) is $Re_\infty = 2.26 \times 10^5$.

B. Computational Fluid Dynamics

1. Computational Methods

Inlet flowfields are computed by using the state-of-the-art commercial solver CFD++ [26], which has been employed by the Australian hypersonics network for scramjet research due to its demonstrated fidelity in hypersonic aerodynamics and aerothermodynamics [8,10,22–25,27]. An implicit algorithm with second-order spatial accuracy is used to solve the Navier–Stokes equations for steady flowfields, and convergence is accelerated by the multigrid technique. Standard air in thermochemical equilibrium state is assumed for the gas, and the inlet surface is assumed to be an isothermal cold wall at 300 K. The inflow is assumed to be fully turbulent and modeled by the two-equation shear-stress transport k-ω Reynolds-averaged Navier–Stokes model due to its demonstrated fidelity in the presence of adverse pressure gradient [28]. Computations are performed until the energy residual is reduced to the order of 10^{-5}, based on a convergence study, where all objective and constraint functions have been found to vary less than 0.07% at higher orders, as seen in Fig. 4, which displays the variations of the deviation of the objective and constraint functions from their converged values (at an energy residual order of 10^{-8}) for the baseline flowfield represented by a coarse mesh.

2. Computational Mesh

Two-dimensional structured meshes are generated by Glyph scripting within the commercial grid generator Pointwise [29] for the inlet geometry defined by the design parameters, as described in Sec. II.A.1 [Meshes are freshly generated from scratch for every individual to be evaluated, according to the design parameter

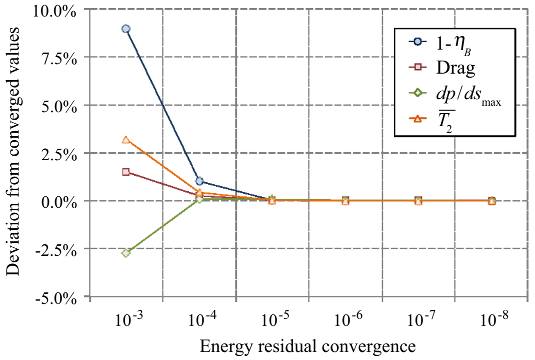

Fig. 4 Convergence of objective and constraint functions (baseline geometry).

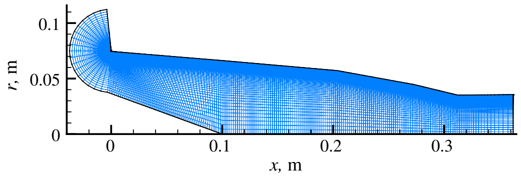

Fig. 5 Computational mesh for the baseline inlet geometry (coarse mesh).

(decision variable) values, not perturbed from the baseline mesh]. The mesh comprises 21,582 cells (219 nodes in the streamwise and 100 nodes in the wall-normal directions) with a nondimensional distance value y^+ of 0.32 on average at the wall surface, as seen in Fig. 5 for the baseline geometry. This mesh resolution has been selected based on a mesh sensitivity study conducted for various resolutions, such as coarse (219 × 100 nodes), nominal (432 × 200 nodes), fine (864 × 400 nodes), and superfine (1728 × 800 nodes) ones. It has been found that, although the coarse mesh can result in up to 9% difference in the compression efficiency η_B, as compared with the superfine one, negligible difference has recorded in the drag and exit temperature (0.7% and 0.04%, respectively), as seen in Table 1. A substantial variation, on the other hand, has been found in the maximum adverse pressure gradient in spite of the essentially similar surface pressure distributions plotted in Fig. 6. This can be attributed to the high sensitivity of the pressure gradient to the local mesh spacing ds, which varies considerably with the mesh resolution, particularly in the vicinity of the compression corners where the meshes are clustered, and it is assumed that a consistent discussion is possible for this quantity among various geometries at a fixed mesh resolution (as is done in Sec. III.B.3). The coarse resolution has thus been selected to minimize the computational cost because the major qualitative tendencies are maintained for the objective and constraint functions owing to the reasonable agreement in the flowfields involving shock wave/boundary layer interactions.

C. Design Optimization

1. *Optimization Algorithms*

The optimization is performed in an iterative manner. Figure 7 schematically shows the optimization chain, which consists of mesh generation (preprocessing), CFD computation (evaluation), post-processing, and optimization algorithms.

Table 1 Mesh sensitivity of objective and constraint functions (baseline geometry)

	$1-\eta_B$	Drag, N	$\frac{dp}{ds_{max}} \times 10^{-6}$, Pa/m	$\bar{T}_2$, K
Coarse	0.2877	134.4	0.7501	738.9
Nominal	0.2880	134.0	1.229	739.7
Fine	0.3135	133.6	3.645	739.2
Superfine	0.3162	133.4	16.26	738.5

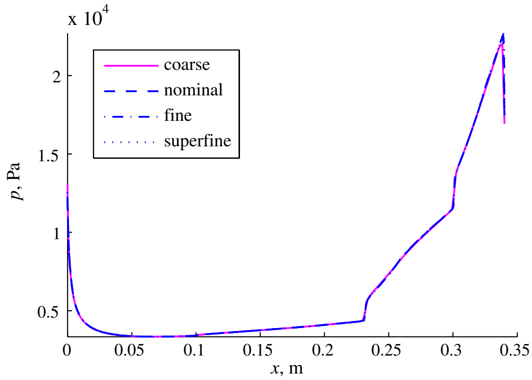

Fig. 6 Comparison of inlet surface-pressure distributions with various mesh resolutions (baseline geometry).

A population-based evolutionary algorithm, in particular, the elitist nondominated sorting genetic algorithm (NSGA-II) [30], is employed for multi-objective design optimization [16,17]. Optimization occurs over 50 generations with 64 individuals in the population pool. A simulated binary crossover and polynomial mutation are used as recombination operators at a given probability (1.0 and 0.1, respectively) with a specified distribution index (10 and 20, respectively). The optimization process is efficiently assisted by replacing CFD evaluations for the objective and constraint functions with the estimations from various surrogate models, including response surface models, kriging approximations, and radial basis functions. Among the predictions from all these models, the one with the least error within a threshold of 10% is adopted to estimate the objective and constraint functions in lieu of actual CFD evaluation, and all individuals that are estimated to be superior to (not dominated by) the present optimums are verified by true CFD evaluation. All members in the population pool are truly evaluated by CFD every five generations, when the surrogate models are trained by using 90% of the solutions from the archive of all truly CFD-evaluated solutions. Variance-based global sensitivity analysis is performed to investigate the influence of the decision variables on the objective and constraint functions, based on the surrogate model with the best prediction accuracy as at the final generation. Evaluation is made for 10,000 sample data points represented by Sobol quasirandom numbers within the decision variable ranges [31,32].

2. *Optimization Problem*

Three characteristic parameters are chosen and used as objective functions to achieve the optimization goal to fulfill the inlet design criteria. The inlet performance is assessed by the compression efficiency, which is defined as the ratio of the enthalpy increase in ideal isentropic compression to that in the actual process, i.e. $\eta_B \equiv [h(p_2, s_1) - h_1]/(h_2 - h_1)$. This parameter is able to account for both shock and viscous losses less sensitively to nonuniform exit flows and inlet heat transfer, as compared with other efficiency parameters [11,12,33]. The inlet drag is evaluated as the second objective function to be minimized. The third objective is to minimize the greatest local adverse pressure gradient on the surface, which if too large would be responsible for boundary-layer separation and unstart (this quantity is treated as an objective function rather than a constraint in the present study because the maximum local adverse pressure gradient that the boundary layer can tolerate without separation has been found to largely depend on the state of the boundary layer [9,34]). A constraint function, a measure of the solution feasibility, is imposed on the mean temperature at the inlet exit (combustor entrance); this is required to be greater than 850 K so that local shock-induced hot structures further downstream can result in autoignition through the effect referred to as radical farming [8,35] because little is known on what constitutes desirable flow profiles at the combustor entrance [11]. The compression efficiency and mean temperature are evaluated by using stream-thrust averaged values [36]. The optimization problem can thus be stated as follows:

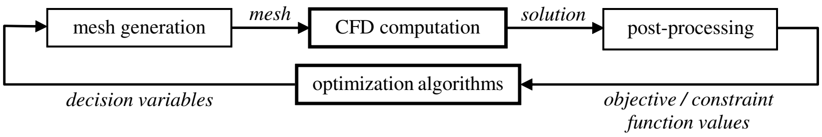

Fig. 7 Optimization loop.

$$\begin{array}{rl} \text{minimize:} & (1)\ 1-\eta_B \\ & (2)\ \text{Drag} \\ & (3)\ \mathrm{d}p/\mathrm{d}s_{\max} \\ \text{subject to:} & \bar{T}_2 \geq 850\ \text{K} \end{array}$$

The ranges of the six decision variables (l_2, l_3, θ_1, $\Delta\theta_2$, $\Delta\theta_3$, and r_c) have been set to allow reasonable geometric variations that are sufficiently large to investigate the influence of the decision variables on the inlet characteristics. The upper and lower bounds are shown later at the top and bottom, respectively, of the columns in Fig. 8.

III. Results

A. Optimization Results

1. *Pareto-Optimal Front*

The optimization has been performed until converged solutions have been achieved, where further evolution has led to little variation in the optimal solutions in the population pool. Figure 9 shows all the individuals (3329 solutions in total) that have been evaluated by CFD up to the 50th generation. The final population is projected on the η_B-$\mathrm{d}p/\mathrm{d}s_{\max}$, Drag-$\eta_B$, and Drag-$\mathrm{d}p/\mathrm{d}s_{\max}$ planes in Fig. 10. The optimal individuals among the feasible solutions form a Pareto-optimal front, which indicates a counteracting trend between the compression efficiency loss 1-η_B and maximum adverse pressure gradient $\mathrm{d}p/\mathrm{d}s_{\max}$ (Fig. 10a). A discrete boundary between the feasible and infeasible solutions according to the exit temperature criterion is found to lie at an approximate drag value of 157 N (Figs. 10b and 10c). Detailed analysis of the behavior follows later in the paper.

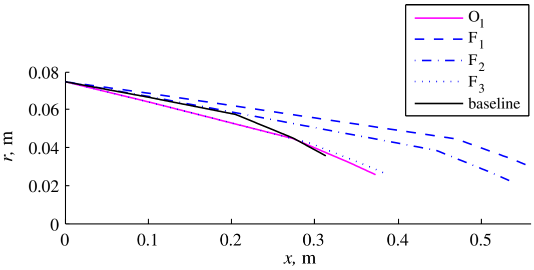

Fig. 8 Objective functions and decision variables for selected individuals.

To investigate the results from the optimization, a few points have been selected that are different in one objective function but similar in the other two, thus facilitating comparison. The values of the objective and constraint functions are shown in Table 2 for such representative cases, and the points are displayed in Fig. 11 along with the 64 nondominated individuals that constitute the Pareto-optimal front (Representative points F_1, F_2 and F_3 are chosen from suboptimal individuals here, contrary to general approaches taken in multi-objective design optimization studies, where comparison is commonly made between multiple optimal points on the Pareto front. This is purposely done in the present research to highlight the effects of geometric features on the resultant inlet performance and facilitate the extraction of useful physical insight into inlet flowfields that is applicable to the design of generic inlets, not limited to the specific conditions and configurations considered in this paper).

The individual O_1 on the Pareto-optimal front has been nominated as the representative optimum owing to its balanced performance in all objective functions (The deviation of O_1 from the minimum of each objective function is 3.5%, 1.1%, and 28.5% for $1-\eta_B$, drag, and $\mathrm{d}p/\mathrm{d}s_{\max}$, respectively, with higher priority given to the compression efficiency and drag rather than the adverse pressure gradient). The feasible individual F_1 offers a similar performance in all aspects, except the compression efficiency η_B. The individual F_2 has similar characteristics to F_1, apart from a greater drag and exit temperature $\bar{T}_2$. The individual F_3, on the other hand, features a performance comparable to O_1, except for a far greater maximum adverse pressure gradient $\mathrm{d}p/\mathrm{d}s_{\max}$. It is notable that the exit temperature $\bar{T}_2$ of O_1 and F_3, which yield lower drag, lies at the verge of the feasibility limit (850 K), whereas that of the baseline geometry does not satisfy the feasibility criterion due to a low exit temperature.

2. *Geometries*

The geometries of the representative individuals are compared in Fig. 12 (not to scale). Plotted in Fig. 8 are the corresponding values of the objective and constraint functions and decision variables, along with the bounding values at the top and bottom of the columns. Considerable variations can be observed in the ramp angle θ_1 and increments $\Delta\theta_{2,3}$ as well as the exit radius r_c among the

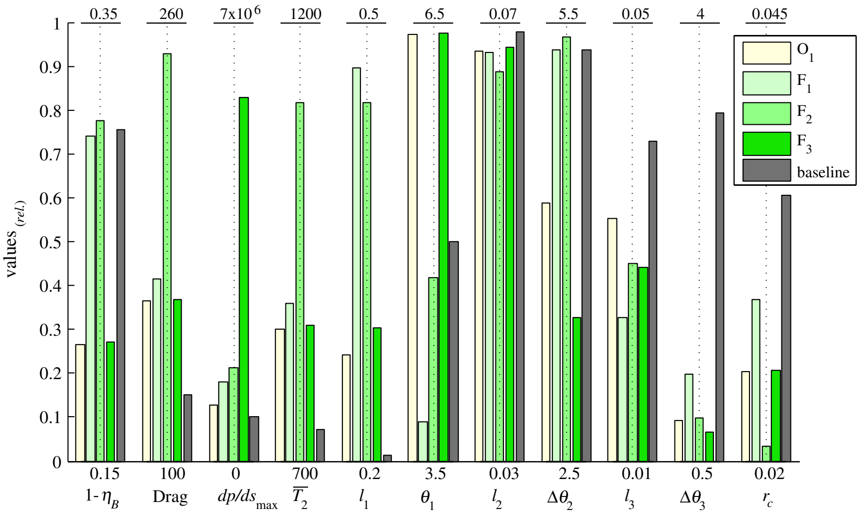

Fig. 9 Optimal population and individuals (50th generation).

representative solutions, whereas the levels of the ramp lengths $l_{2,3}$ are relatively similar. The total inlet length varies accordingly in response to the variation of the ramp angles. The effects of the geometric characteristics on the performance criteria are discussed in detail in the following sections.

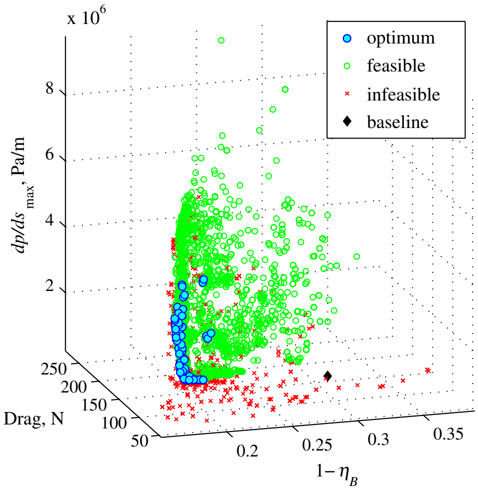

Fig. 10 Population projections on objective function planes.

Table 2 Objective and constraint function values of the representative points

	$1-\eta_B$	Drag, N	$\frac{dp}{ds_{\max}}$, Pa/m	$\bar{T}_2$, K
O_1	0.203	158	8.95×10^5	850
F_1	0.298	167	1.27×10^6	879
F_2	0.305	249	1.48×10^6	1108
F_3	0.204	159	5.80×10^6	855
Baseline	0.301	124	7.13×10^5	736

B. Observations

1. Compression Efficiency

The definition of the compression efficiency η_B can be re-written as $\eta_B \equiv [h(\bar{T}_{2_{\text{isen}}}) - h(\bar{T}_1)]/[h(\bar{T}_2) - h(\bar{T}_1)]$, where $\bar{T}_{2_{\text{isen}}} = (\bar{p}_2/\bar{p}_1)^{(\bar{\gamma}-1)/\gamma}\bar{T}_1$ according to the isentropic relations. For a given set of $\bar{T}_1$ and $\bar{T}_2$, by this definition, the compression efficiency η_B becomes larger for greater $\bar{p}_2/\bar{p}_1$. The maximum efficiency of 100% is attained when the compression process is isentropic because the flow can hold the maximum possible static pressure at the exit in the absence of any total pressure loss. This parameter thus indicates how efficiently compression has been achieved for a certain temperature rise between the inlet entrance and exit.

Figure 13 compares the compression efficiency for the representative geometries. O_1 and F_3 are found to yield higher compression efficiency in comparison with $F_{1,2}$ and the baseline

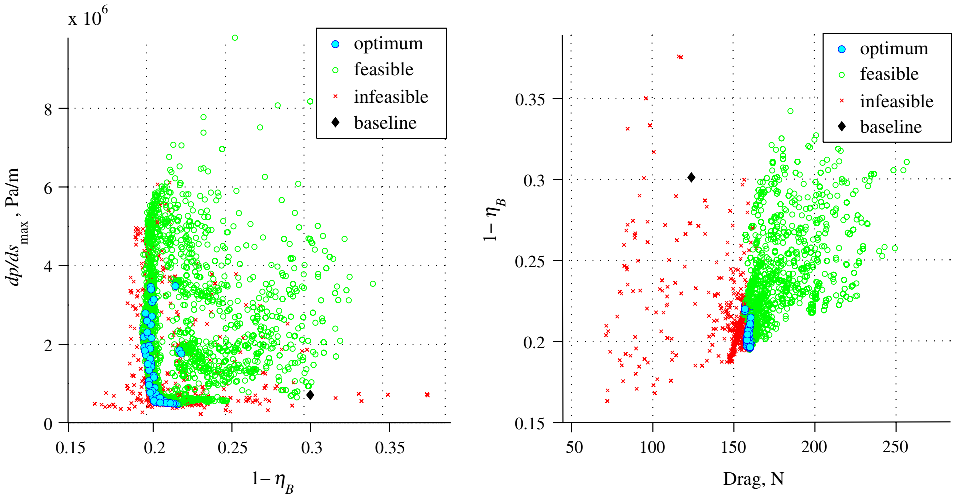

a) $\eta_B - dp/ds_{\max}$ plane b) Drag – η_B plane

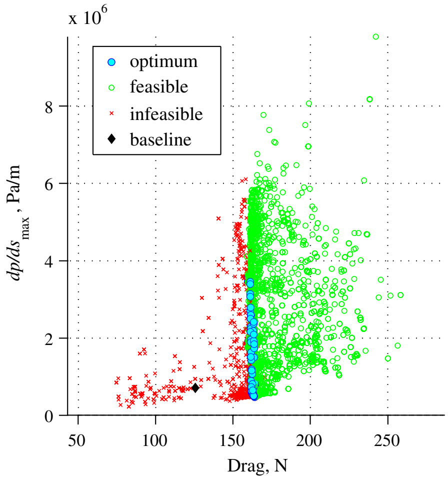

c) Drag – $dp/ds_{\max}$ plane

Fig. 11 Pareto-optimal front and representative points.

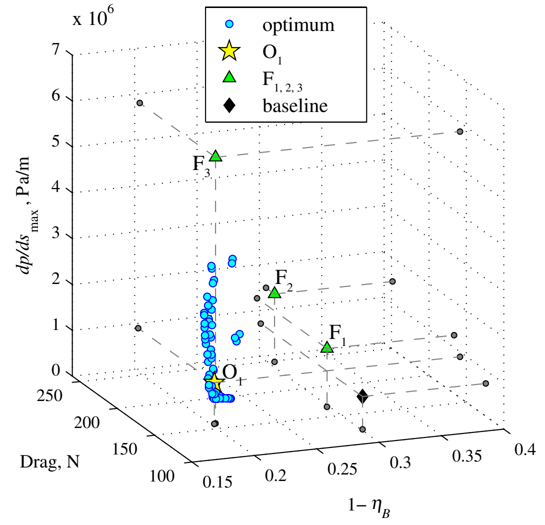

Fig. 12 Geometries of selected individuals.

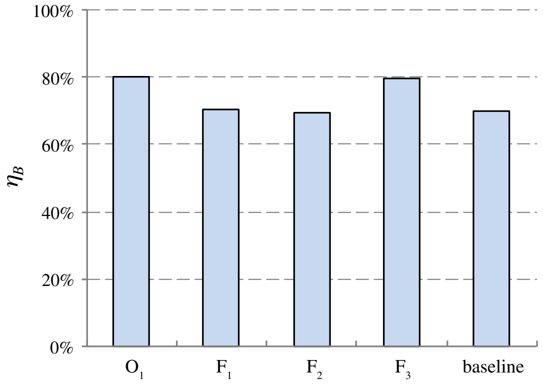

Fig. 13 Compression efficiency.

geometry. The flowfield of O_1 is compared with that of the baseline in Fig. 14.

Plotted in Fig. 15 are the stream-thrust-average static temperature and pressure for the representative geometries, along with the isentrope curve shown by a dashed line. The deviation from the isentrope line is found to be smaller for the O_1 and F_3 geometries, indicating that inlet compression is achieved with less entropy increase, hence total pressure loss for these cases, as compared with the other geometries, whose pressure falls onto the dotted trend line. This corresponds with the tendency observed in Fig. 13. It is notable that the average static pressure $\bar{p}_2$ achieved by F_1 is considerably lower than that achieved by O_1 and F_3, although similar compression levels have been achieved in terms of the static temperature $\bar{T}_2$ (850–880 K) for these three cases. The static temperature and pressure profiles at the inlet exit plotted in Fig. 16 show considerably lower values for F_1, compared with those for O_1 and F_3, accordingly.

The flowfields for the O_1 and F_1 geometries are compared in Fig. 14 with respect to the Mach number and temperature. The O_1 flowfield is characterized by the impingement of the first reflected shock on the expansion corner at the junction of the inlet and combustor, which effectively allows the majority of flow compression to complete within the inlet, whereas the reflected shock wave impinges on the second inlet ramp, and flow compression occurs even in the combustor section in the case of the F_1 flowfield. According to the inviscid theory for axisymmetric flowfields, the so-called full Busemann inlet [37] is able to compress the airflow with a minimum entropy rise in case the inner inlet wall is represented by a fully concave surface as in the present study. Compression is achieved by means of isentropic compression through a series of Mach waves and a sole entropy jump across a terminating conical shock wave, as schematically shown in Fig. 17. It can be noted that the O_1 geometry is akin to the full Busemann inlet despite the presence of viscous effects and compression via a finite number of ramps, being able to fulfill the compression requirement of $\bar{T}_2 \geq 850$ K with a minimum compression efficiency loss, whereas the shock waves originating from the second and third compression corners play a secondary role with a minor influence on the flow compression process.

2. *Drag*

The inlet drag is compared in Fig. 18, including the breakdown of the pressure (inviscid) and viscous contributions, which can be obtained by integrating the pressure and shear stress along the surface as $\text{Drag} = D_{\text{pres}} + D_{\text{visc}} = \int_s (p \sin\theta + \tau \cos\theta) 2\pi r \, ds$. The distributions of $p \sin\theta$ and $\tau \cos\theta$ along the inlet surface are plotted in Fig. 19.

The higher drag level incurred by O_1 compared with the baseline can primarily be attributed to a smaller exit radius r_c, i.e., an increased projected wall area on which the pressure can act in the x direction. A somewhat higher drag is incurred by F_1, where the viscous contribution is augmented by a larger skin friction drag on the extended inlet surface, as seen in Figs. 14 and 19b. Nearly the same level of pressure drag, on the other hand, is incurred by O_1 and F_1 despite a larger frontal area of O_1, which is attributed to the higher pressure acting on a large extent of the second and third ramp due to the impingement of the main shock reflected on the symmetry axis in the F_1 flowfield (Figs. 14 and 19a). The greatest drag is experienced by F_2 due to its smallest exit radius r_c and hence the largest frontal area, whereas the viscous drag is comparable to F_1 due to a similar inlet length (Fig. 19b).

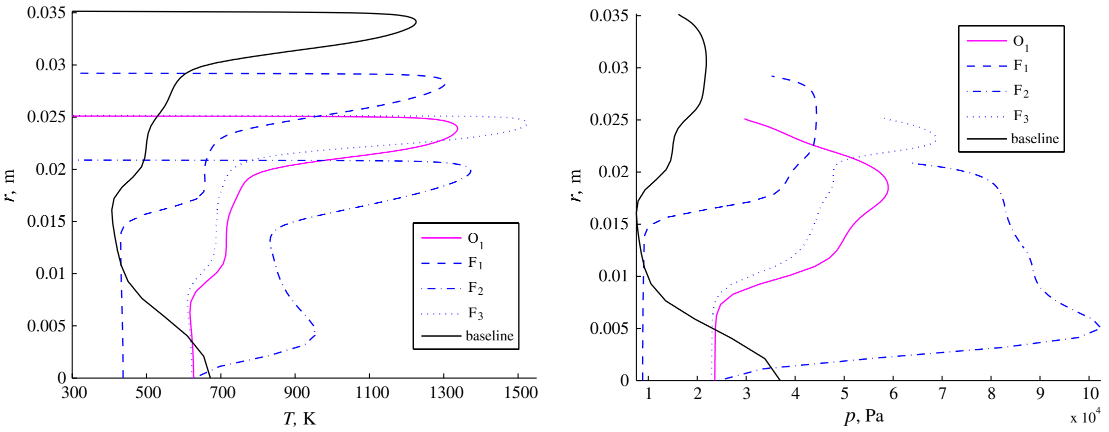

a) Temperature **b) Pressure**

Fig. 14 Mach number distributions of O_1 and F_1 geometries.

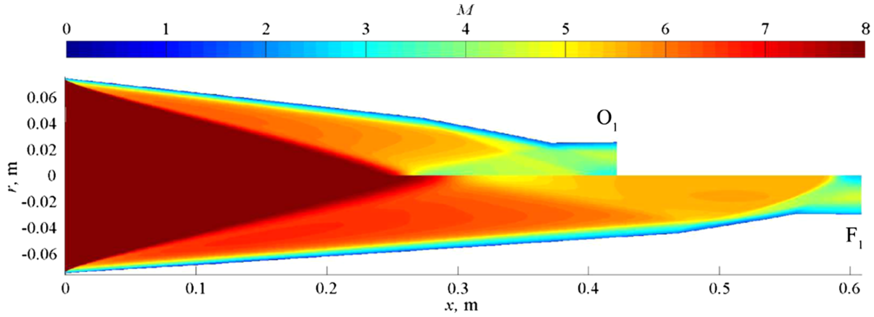

Fig. 15 Temperature and pressure at inlet exit.

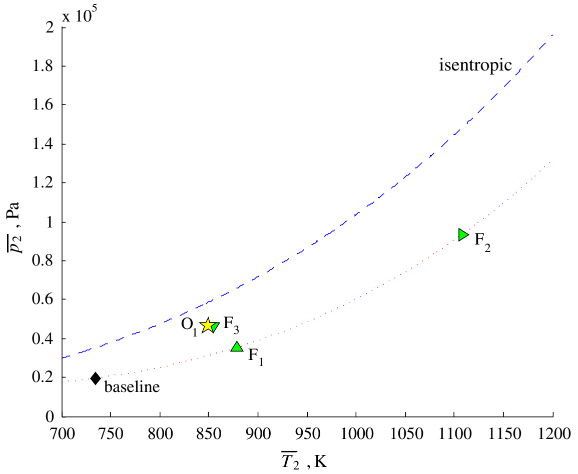

Fig. 16 Flow profiles at the inlet exit.

3. *Pressure Gradient*

An adverse pressure gradient is a primary factor that is responsible for incipient flow separation and thus is minimized as one of the objective functions rather than a constraint because the degree of gradient that the boundary layer can withstand without separation is dependent on various factors such as the flow viscosity, turbulent kinetic energy, and thermal treatment of the wall surface [9,34]. It has been found in Fig. 11 that F_3 is subject to a substantially higher degree of adverse pressure gradient, compared with the O_1 geometry, wheras the compression efficiency and drag levels are virtually the same for both.

The flowfields are compared in Fig. 20, where both geometries appear to be very similar. However, the wall pressure distributions plotted in Fig. 21 show a perpendicular rise immediately upstream of the inlet end in the F_3 case, which has led to an acute adverse gradient. This can be attributed to a smaller increment of the second ramp $\Delta\theta_2$ of F_3. It renders the third ramp to extend slightly further downstream, where the reflected conical shock wave impinges, subsequently causing a large pressure gradient, which was felt by F_3 but avoided by O_1. The shock structure of the full Busemann inlet (Fig. 17) is advantageous not only for the compression efficiency but also in this aspect, preventing the shock impingement of the reflected shock upon the inner inlet wall, although particular care ought to be taken under off-design conditions. The highly localized, abrupt behavior of the pressure gradient observed here highlights the particular effectiveness of population-based global search, in contrast to gradient-based local search, for which the detection of the global optimum would be formidable if search were started with an unfavorable initial point in the nonsmooth design space.

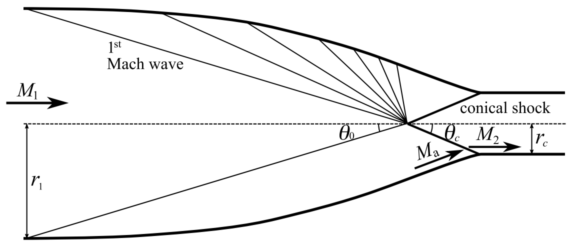

Fig. 17 Full Busemann inlet [38].

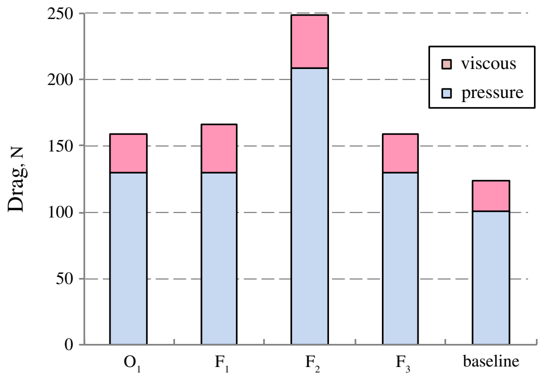

Fig. 18 Drag comparison and breakdown.

4. *Temperature at Exit*

The flow temperature at the inlet exit plays a key role in the ignition process in the combustion chamber, particularly for radical-farming shock-induced combustion, where a sufficient amount of heat release is required to produce radicals and induce combustion [7,8]. The stream-thrust average of the exit temperature is thus employed as a constraint function to judge the feasibility of the individuals. The

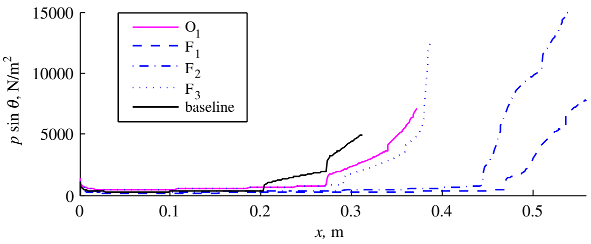

a) Pressure force

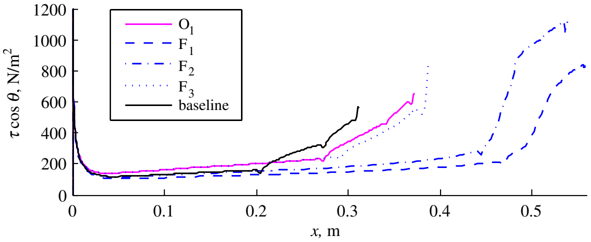

b) Shear stress

Fig. 19 Comparison of pressure and shear stress contributions to drag.

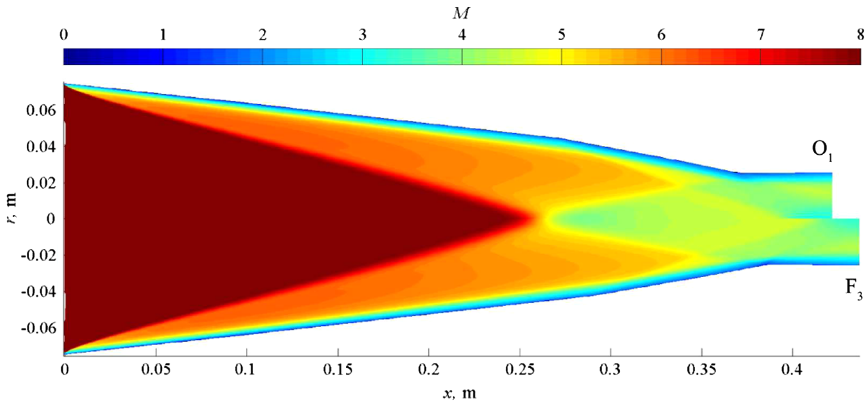

Fig. 20 Mach number distributions of O_1 and F_3 geometries.

temperature profiles at the inlet exit are compared in Fig. 15, and the temperature distributions are displayed in Fig. 22.

The feasible solutions are found to have satisfied the temperature requirement for self-ignition ($\bar{T}_2 \geq 850$ K) in various ways; F_1 has cleared the minimum temperature criterion with a relatively large exit radius r_c owing to the near-wall high temperature zone as seen in the thermal boundary layer in Figs. 16a and 22a. F_2, on the other hand, has attained a high temperature of $\bar{T}_2 = 1108$ K, well over the self-ignition temperature, with high compression with a smaller radius close to the lower bound of the r_c range, which has led to the emergence of an additional localized high-temperature region near the axis of symmetry (Fig. 22b), although it makes insignificant contribution to the stream-thrust-average temperature due to its proximity to the axis. O_1 and F_3 lie in the middle, the latter of which has a narrower and higher peak due to a slight modification of the shock structure caused by a smaller value of $\Delta\theta_2$.

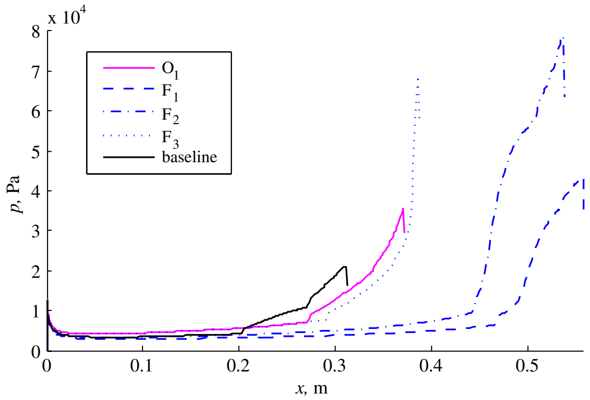

Fig. 21 Wall-pressure distributions.

It has been noted in the projection plots of the final population and individuals (Figs. 10b and 10c) that the feasibility of the solutions distinctly changes across a certain level of drag (157 N), suggesting the existence of a correlation between the drag and exit temperature. An analytical study has been conducted to elucidate the trend observed here: the inlet drag can be expressed as the difference in the stream thrust (momentum) between the incoming and outgoing airflows, i.e., Drag $= F_{\mathrm{in}} - F_{\mathrm{in}}$, according to the momentum balance theory. Coupling the definitions of the mass flow $\dot{m} = \bar{\rho}\,\bar{U}A$ and

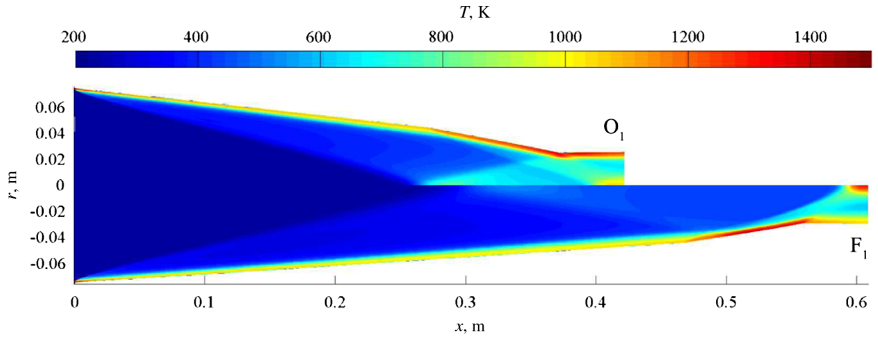

a) O_1 and F_1

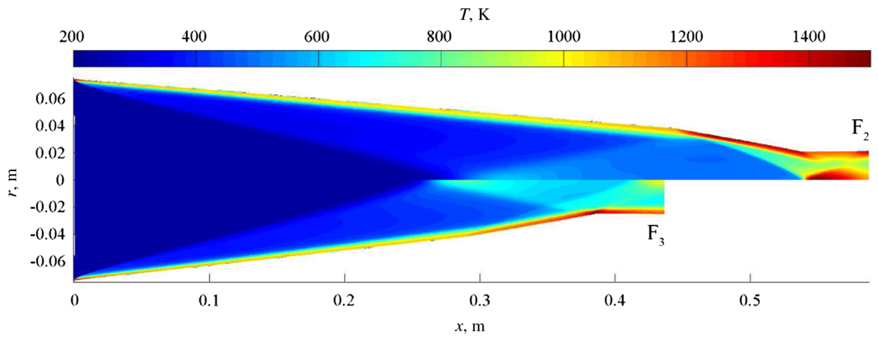

b) F_2 and F_3

Fig. 22 Temperature distributions.

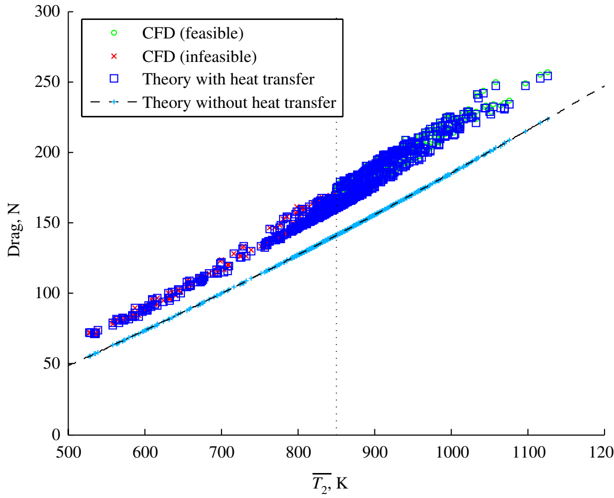

Fig. 23 Inlet drag comparison with respect to exit temperature between CFD and theory.

stream thrust $F_{\text{out}} = (\bar{p} + \bar{\rho}\bar{U}^2)A$ with the energy balance equation $h_t + \Delta Q/\dot{m} = \bar{h}_2 + 1/2\bar{U}^2$, a mathematical expression can be derived for the inlet drag in terms of the exit temperature:

$$\text{Drag} = F_{\text{in}} - \dot{m}\frac{2(h_t + \Delta Q/\dot{m} - \bar{h}_2) + R\bar{T}_2}{\sqrt{2(h_t + \Delta Q/\dot{m} - \bar{h}_2)}} \tag{1}$$

where ΔQ is the heat transfer across the inlet surface, and the static enthalpy $\bar{h}_2$ is a function of the inlet exit temperature $\bar{T}_2$ for the thermally equilibrium air assumed in this study.

Figure 23 compares the CFD solutions evaluated during the optimization with theoretical results. The dashed line is the analytical curve obtained from Eq. (1) by assuming no heat transfer ($\Delta Q = 0$) for a given inflow ($F_{\text{in}} = 1901$ N, $\dot{m} = 0.786$ kg/s, and $h_t = 3.15$ MJ/kg), whereas the squares denote the solutions obtained by substituting the heat transfer values calculated numerically in CFD into ΔQ in Eq. (1). The close agreement between the squares and CFD solutions with an rms error of 0.32% reassures that the deviation of the CFD results from the dashed analytical curve solely originates from the surface-heat transfer, which accounts for 15.7% drag increase on average, compared with the drag in the absence of heat transfer (in other words, the inlet drag can be expressed as a function of the exit temperature only in the case of adiabatic inlet walls).

5. *Sensitivity Analysis*

Global sensitivity analysis has been performed, based on the prediction from the best surrogate model with the least error that has been trained by using the archive of the CFD solutions evaluated in the course of the optimization [15,31]. The first-order sensitivity index S represents the main effect of the input parameter (decision variable) on the output parameter (objective/constraint function). The total sensitivity index S_T is the sum of all the effects, including first-order as well as higher-order ones, which account for the interactions with the other parameters. A small S_T value indicates that the parameter is noninfuential and can be fixed anywhere in its distribution without affecting the variance of the output [31].

The sensitivity indices S and S_T are plotted in Fig. 24 for the compression efficiency η_B, whose indices are found to be very similar to those for the drag and exit temperature $\bar{T}_2$ (No reasonable indices have been obtained for the maximum adverse pressure gradient $\mathrm{d}p/\mathrm{d}s_{\max}$ due possibly to the highly local nature of this parameter, as compared with the others, which are integral quantities). It can be seen that the radius at the inlet exit r_c exerts dominant influence on these objective and constraint functions. The ramp angles and lengths have a rather minor influence, but the former can exert more impact in conjunction with other parameters, as indicated by their larger proportions in S_T than in S.

This result is consistent with the observation that the compression efficiency can be maximized by geometries akin to the full Busemann inlet, where the following relation holds for the overall inlet length and other geometric parameters according to Fig. 17: $l_1 + l_2 + l_3 = r_1/\tan\theta_0 + r_c/\tan\theta_c$, where r_1 is constant at 0.075 m, and θ_0 is determined by the inflow Mach number M_1 and the first ramp angle θ_1 in the present study. The total inlet length is thus expressed as a function of r_c and θ_c, which is determined in relation to the exit Mach number $\bar{M}_2$. The inlet exit radius r_c can then be directly correlated with the exit temperature $\bar{T}_2$ and surface-heat transfer ΔQ due to the energy balance equation $h_t + \Delta Q/\dot{m} = \bar{h}_2 + 1/2\bar{M}_2^2\gamma R\bar{T}_2$. This correlation makes r_c a key factor in determining the compression efficiency, inlet drag, and exit temperature as a consequence.

6. *Summary*

The insight gained into axisymmetric scramjet inlet flowfields as a result of the present study is summarized here:

1) The inlet exit radius (or contraction ratio) has the most dominant effect on the compression efficiency, inlet drag, and exit temperature among all design parameters. The ramp angles have secondary influence on these design criteria, which are little affected by the ramp length.

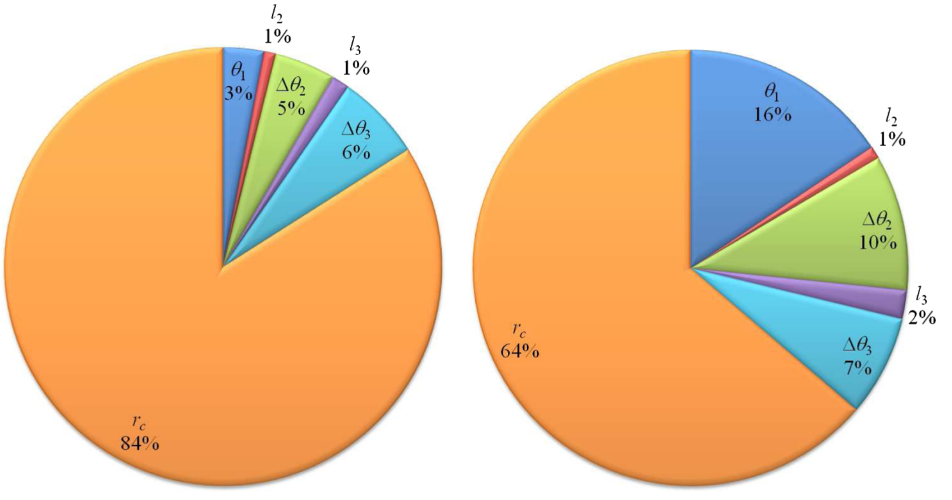

a) First-order sensitivity index S **b) Total sensitivity index S_T**

Fig. 24 Global sensitivity analysis on η_B.

2) Both compression efficiency losses and abrupt adverse pressure gradient (hence boundary-layer separation) can be prevented effectively by employing Busemann-type flow structures characterized by initial isentropic compression followed by a terminating conical shock wave, which impinges on the junction of the inlet and combustor.

3) The inlet drag is directly linked with the exit temperature with secondary influence of heat transfer across the inlet surface (or no influence in case of adiabatic surface), indicating a monotonic increase of the inlet drag as a function of the exit temperature.

This insight consequently provides the following remarks that can be applied to the design of axisymmetric inlets:

4) High inlet performance can be achieved by Busemann-type geometries with necessary modifications, including truncation, multiple ramps, and corrections, for boundary/shock layers, in accordance with the requirements.

5) The inlet drag can be reduced by mitigating the minimum temperature requirement at the inlet exit (or combustor entrance) and further reduction (up to 15.7% in the present study) can be achieved by suppressing surface-heat transfer.

IV. Conclusions

A multi-objective design optimization has been performed for axisymmetric scramjet inlets with respect to four design criteria, namely, the compression efficiency, drag and maximum adverse pressure gradient as objective functions, and the exit temperature as a constraint function. The inlet geometry comprising three compression ramps has been optimized by coupling surrogate-assisted evolutionary algorithms and a computational fluid dynamics solver for viscous equilibrium flowfields, resulting in a Pareto-optimal front. The flowfields have been scrutinized for the representative cases, and sensitivity analysis has been applied to the stored solution archive by using the trained surrogate models.

The inlet exit radius is found to be the most influential parameter on the compression efficiency, inlet drag, and exit temperature. Busemann-type geometries are advantageous in maximizing the compression efficiency while preventing abrupt adverse pressure gradient, which can potentially induce unfavorable flow separation. The inlet drag has been found to be determined primarily by the exit temperature and secondarily by the surface-heat transfer for inlets with fixed mass flow capture. These results suggest that the inlet can be designed in a decoupled manner for given combustor specifications and that the inlet drag need not be considered as an objective function to minimize if the minimum temperature is specified at the combustor entrance, simplifying the overall scramjet design process.

Acknowledgment

The authors are grateful to Tapabrata Ray and Amitay Isaacs at the University of New South Wales for providing the advanced multi-objective design optimization capability developed in the group.

References

[1] Paull, A., Alesi, H., and Anderson, S., “HyShot Flight Program and How it was Developed,” AIAA Paper 2002-5248, Sept. 2002.

[2] Boyce, R. R., Gerard, S., and Paull, A., “The HyShot Scramjet Flight Experiment—Flight Data and CFD Calculations Compared”, AIAA Paper 2003-7029, Dec. 2003.

[3] McClinton, C. R., “X-43—Scramjet Power Breaks the Hypersonic Barrier: Dryden Lectureship in Research for 2006”, AIAA Paper 2006-1-317, Jan. 2006.

[4] Boeing, “X-51A WaveRider Breaks Record in 1st Flight”, *News Releases/Statements* [online database], http://boeing.mediaroom.com [retrieved 26 May 2010].

[5] Boyce, R. R., Tirtey, S. C., Brown, L., Creagh, M., and Ogawa, H., “SCRAMSPACE : Scramjet-based Access-to-Space Systems”, AIAA Paper 2011-2297, Apr. 2011.

[6] Hunt, D. C., Paull, A., Boyce, R. R., and Hagenmaier, M., “Investigation of an Axisymmetric Scramjet Configuration Utilizing Inlet-Injection and Radical Farming”, *Proceedings of the 19th International Symposium on Airbreathing Engines (ISABE 2009)*, ISABE Paper 2009-1353, Montreal, QC, Canada, Sept. 2009.

[7] Odam, J., and Paull, A., “Radical Farming in Scramjets,” *Notes on Numerical Fluid Mechanics and Multidisciplinary Design*, Vol. 96 edited by C. Tropea, S. Jakirlic, H. J. Heinemann, and H. Hinlinger, Springer–Verlag, Berlin/New York/Heidelberg, 2007.

[8] McGuire, J. R., Boyce, R. R., and Mudford, N. R., “Radical Farm Ignition Processes in Two-dimensional Supersonic Combustion”, *Journal of Propulsion and Power*, Vol. 24, No. 6, 2008, pp. 1248–1257. doi:10.2514/1.35562

[9] Ogawa, H., Grainger, A. L., and Boyce, R. R., “Numerical Investigation of Viscous Effects on Scramjet Inlet Starting,” in *Proceedings of 2009 Asia-Pacific International Symposium on Aerospace Technology*, JSASS, Gifu, Japan, Nov. 2009.

[10] Ogawa, H., Grainger, A. L., and Boyce, R. R., “Inlet Starting of High-Contraction Axisymmetric Scramjets”, *Journal of Propulsion and Power*, Vol. 26, No. 6, 2010, pp. 1247–1258. doi:10.2514/1.48284

[11] Van Wie, D. M., “Scramjet Inlets,” *Scramjet Propulsion*, Progress in Astronautics and Aeronautics, Vol. 189, edited by E. T. Curran, and Murthy, S. N. B, AIAA, Reston, VA, 2000.

[12] Matthews, A. J., “Scramjet Intakes,” Ph.D. Dissertation, Univ. of Oxford, Oxford, England, U.K., 2003.

[13] Deb, K., *Multiobjective Optimization Using Evolutionary Algorithms*, Wiley, New York, 2001.

[14] Forrester, A., Sobester, A., and Keane, A., *Engineering Design via Surrogate Modelling: A Practical Guide*, Wiley, Hoboken, NJ, 2008.

[15] Queipo, N. V., Haftka, R. T., Shyy, W., Goel, T., Vaidyanathan, R., and Tucker, P. K.,“Surrogate-Based Analysis and Optimization”, *Progress in Aerospace Sciences*, Vol. 41, 2005, pp. 1–28. doi:10.1016/j.paerosci.2005.02.001

[16] Ray, T., and Smith, W., “A Surrogate Assisted Parallel Multiobjective Evolutionary Algorithm for Robust Engineering Design,” *Engineering optimization*, Vol. 38, No. 8, 2006, pp. 997–1011. doi:10.1080/03052150600882538

[17] Ray, T., Isaacs, A., and Smith, W., “Multi-Objective Optimization Using Surrogate-Assisted Evolutionary Algorithm”, *Multi-Objective Optimization: Techniques and Applications in Chemical Engineering*, World Scientific, Singapore, 2008, pp. 131–151.

[18] Knill, D. L., Giunta, A. A., Baker, C. A., Grossman, B., Mason, W. H., Haftka, R. T., and Watson, L. T., “Response Surface Models Combining Linear and Euler Aerodynamics for Supersonic Transport Design,” *Journal of Aircraft*, Vol. 36, No. 1, 1999, pp. 75–86. doi:10.2514/2.2415

[19] Papila, N., Shyy, W., Griffin, L., and Dorney, D. J., “Shape Optimization of Supersonic Turbines Using Global Approximation Methods,” *Journal of Propulsion and Power*, Vol. 18, No. 3, 2002, pp. 509–518. doi:10.2514/2.5991

[20] Kanazaki, M., Tanaka, K., and Yamamoto, K., “Multi-objective Aerodynamic Optimization of Elements Setting for High-lift Airfoil Using Kriging Model”, AIAA Paper 2006-1471, Jan. 2006.

[21] Deepak, N. R., Ray, T., and Boyce, R. R., “Shape Optimization of the Nose Cone for a Hypersonic Flight Experiment Trajectory,” *Journal of Spacecraft and Rockets*, Vol. 45, No. 3, 2008, pp. 428–437. doi:10.2514/1.33826

[22] Ogawa, H., and Boyce, R. R., “Physical Insight into Scramjet Inlet Behavior via Multi-Objective Design Optimisation”, in *Proceedings of International Council of the Aeronautical Sciences (ICAS) 2010 Congress*, ICAS, Nice, France, Sept. 2010.

[23] Ogawa, H., and Boyce, R. R., “Physical Insight into Nozzle Flow Behavior of Axisymmetric Scramjets for Access-to-Space via Design Optimization”, *Proceedings of the 10th Australian Space Science Conference*, ASSC, Brisbane, Australia, Sept. 2010.

[24] Ogawa, H., Alazet, Y., Pudsey, A., Boyce, R. R., Isaacs, A., and Ray, T., “Full Flow-Path Optimization of Axisymmetric Scramjet Engines”, AIAA Paper 2011-2347, Apr. 2011.

[25] Ogawa, H, Brown, L, Boyce, R. R., and Ray, T., “Multi-Objective Design Optimisation of Axisymmetric Scramjet Nozzle and External Components Considering Static Stability by Using Surrogate-Assisted Evolutionary Algorithms”, in *Proceedings of the 20th International Society for Airbreathing Engines (ISABE 2011)*, ISABE Paper 2011-1513, Göteborg, Sweden, Sept. 2011.

[26] CFD++, Software Package, Ver. 8.11, Metacomp Technologies, Inc., Agoura Hills, CA, 2009.

[27] Goldberg, U., Peroomian, O., Chakravarthy, S., and Sekar, B., “Validation of CFD++ Code Capability for Supersonic Combustor Flowfields”, AIAA Paper 1997-3271, July 1997.

[28] Bardina, J. E., Huang, P. G., and Coakley, T. J., “Turbulence Modeling Validation, Testing, and Development”, NASA TM 110446, 1997.

[29] Pointwise, Software Package, Ver. 16.02, Pointwise, Inc., Fort Worth, TX, 2008.

[30] Deb, K., Pratap, A., Agarwal, S., and Meyarivan, T., "A Fast and Elitist Multiobjective Genetic Algorithm: NSGA-II", *IEEE Transactions on Evolutionary Computation, Vol. 1, No. 1*, Vol. 6, No. 2, 2002, pp. 182–197.
doi:10.1109/4235.996017

[31] Saltelli, A., Ratto, M., Andres, T., Compolongo, F., Cariboni, J., Gatelli, D., Saisana, M., and Tarantola, S., *Global Sensitivity Analysis. The Primer*, Wiley, Hoboken, NJ, 2008.

[32] Sobol, I. M., "Uniformly Distributed Sequences with Additional Uniformity Properties," *USSR Computational Mathematics and Mathematical Physics* , Vol. 16, No. 5, 1976, pp. 236–242.
doi:10.1016/0041-5553(76)90154-3

[33] Billig, F. S., and Van Wie, D. M., "Efficiency Parameters for Inlets Operating at Hypersonic Speeds," in *Proceedings of the 8th International Symposium on Airbreathing Engines*, ISABE Paper 1987-7047, Cincinnati, OH, June 1987.

[34] Ogawa, H., and Boyce, R. R., "Numerical Investigation of Turbulent Effects on Boundary Layer Separation in Axisymmetric Scramjet Inlets via Design Optimization," in *Proceedings of the 7th International Conference of Flow Dynamics*, GCOE, Sendai, Japan, Nov. 2010.

[35] Paull, A., and Stalker, A. J., "Scramjet Testing in the T3 and T4 Hypersonic Impulse Facilities", *Scramjet Propulsion*, Progress in Astronautics and Aeronautics, edited by E. T. Curran, and Murthy, S. N. B., Vol. 189, AIAA, Reston, VA, 2000.

[36] Mölder, S., and McGregor, R. J., "Analysis and Optimization of Scramjet Inlet Performance," *Proceedings of the 17th Congress of the Aeronautical Sciences*, ICAS Paper 1990-4.7.3, Stockholm, Sweden, Sept. 1990.

[37] Busemann, A., "Die Achsensymmetrische Kegelige Überschallströmung," *Luftfahrtforschung*, Vol. 19, 1942, pp. 137–144.

[38] Billig, F. S., Baurle, R. A., Tam, C.-J., and Wornom, S. F. "Design and Analysis of Streamline Traced Hypersonic Inlets", AIAA Paper 1999-4974, 1999.

J. Martins
Associate Editor